Design of a lightweight and slender hyper-redundant manipulator for underwater applications

Poka, Ardit; Ludovico, Daniele; Manara, Federico; De Mari Casareto Dal Verme, Lorenzo; Canali, Carlo; Berselli, Giovanni; Caldwell, Darwin G.; Jovanova, Jovana

DOI
10.1016/j.oceaneng.2025.122800

Publication date
2025

Document Version
Final published version

Published in
Ocean Engineering

Citation (APA)
Poka, A., Ludovico, D., Manara, F., De Mari Casareto Dal Verme, L., Canali, C., Berselli, G., Caldwell, D. G., & Jovanova, J. (2025). Design of a lightweight and slender hyper-redundant manipulator for underwater applications. *Ocean Engineering*, *342*, Article 122800. https://doi.org/10.1016/j.oceaneng.2025.122800

Ocean Engineering 342 (2025) 122800

Contents lists available at ScienceDirect

Ocean Engineering

journal homepage: www.elsevier.com/locate/oceaneng

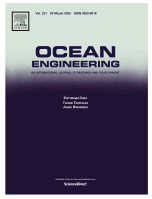

Research paper

Design of a lightweight and slender hyper-redundant manipulator for underwater applications

Ardit Poka [a,b,c,*], Daniele Ludovico [a], Federico Manara [a,b,d], Lorenzo De Mari Casareto Dal Verme [a], Carlo Canali [a,d], Giovanni Berselli [a,b], Darwin G. Caldwell [a], Jovana Jovanova [c]

[a] Advance Robotics (ADVR), Istituto Italiano di Tecnologia (IIT), Via Morego, 30, Genova, 16163, Italy
[b] Dipartimento di Ingegneria Meccanica, Energetica, Gestionale e dei Trasporti (DIME), Universitá di Genova, Via Balbi 5, Genova, 16126, Italy
[c] Maritime and Transport Technology (M& TT), Delft University of Technology, Mekelweg 5, Delft, 2628 CD, Netherlands
[d] RAISE Ecosystem, Genova, 16126, Italy

ARTICLE INFO

Keywords:
Underwater
Robot
Manipulator
Hyper-redundant
Cable-driven
Design
Optimisation

ABSTRACT

Hyper-redundant manipulators offer high dexterity and manoeuvrability in constrained environments, yet their design must integrate structural efficiency with environmental adaptability. This study presents a co-design framework for lightweight, cable-driven hyper-redundant manipulators optimised for underwater applications, such as the usage in combination with a Remotely Operated Vehicle. Building on a modular architecture of an eight-degree-of-freedom cable-driven manipulator, the methodology integrates Gaussian process regression-based stress prediction and generative design to achieve mass and size reductions, as well as a hydrodynamically efficient shape while ensuring structural integrity under extreme static loads. A 3D-printed module fabricated from Onyx, a carbon fibre-reinforced nylon, achieved near-neutral buoyancy in seawater, validated through submerged testing of a two-module prototype. An external buoyant element design was then provided for manipulators with no inherent buoyancy, accounting for printability, density mismatch between actual and theoretical density, and joint range of motion. This work advances underwater hyper-redundant robot design by combining data-driven optimisation with modular buoyancy strategies and hydrodynamic efficiency, providing a scalable method for fluid environments.

1. Introduction

Hyper-Redundant (HR) manipulators, with their high Degrees Of Freedom (DOF) and bioinspired adaptability, are advanced robotic systems designed for confined and unpredictable environments (Manara et al., 2025; Poka et al., 2025b; Zhao et al., 2020). These systems excel in tasks requiring precision, slenderness, and manoeuvrability, particularly in constrained settings where traditional bulky robots face inherent limitations, such as inspection and maintenance (Canali et al., 2022), search and rescue (Yamauchi et al., 2022), and minimally invasive surgery (Clark et al., 2015; Rout et al., 2020). These robots have been studied extensively for the mentioned terrestrial applications. However, not as much research has been done on offshore applications, marine technology and underwater environments (Poka et al., 2025a). Traditional underwater robotic systems, such as Autonomous Underwater Vehicles (AUVs) and Remotely Operated Vehicles (ROVs), play a crucial role in subsea maintenance, repair, and inspection (Aguirre-Castro et al., 2019; Zhou et al., 2023). However, these technologies often struggle with the precision and adaptability needed to operate effectively in tight spaces, such as between closely spaced underwater pipelines or within shipwrecks (Birk et al., 2018). Underwater snake-like robots can be useful to overcome these challenges. They are designed to mimic the flexibility and agility of natural creatures like sea snakes and eels, which excel at navigating confined and unpredictable environments (Sverdrup-Thygeson et al., 2017). Their adaptable, elongated, and highly manoeuvrable structures make them well-suited for tasks such as inspection and maintenance in offshore energy installations (Liljebäck and Mills, 2017; Lyu et al., 2022). Unlike conventional ROVs or AUVs, these robots can access hard-to-reach areas, including the interiors of complex underwater structures, where traditional systems would struggle. Underwater applications, from marine exploration to subsea infrastructure maintenance, can benefit from manipulators that combine slender geometries with structural robustness, all while compensating for buoyancy imbalances and water resistance (Zheng et al., 2013; Tang et al., 2019; Sitler and Wang, 2022). Achieving such a balance remains an open challenge, highlighting the need for new optimisation frameworks. This study

* Corresponding author.
E-mail address: arditpoka@live.it, ardit.poka@iit.it (A. Poka).

https://doi.org/10.1016/j.oceaneng.2025.122800
Received 18 March 2025; Received in revised form 26 August 2025; Accepted 9 September 2025
Available online 20 September 2025

addresses these challenges by designing and developing a tendon-driven, modular HR manipulator optimised for underwater deployment. The aim is to design an underwater manipulator that can be attached to an ROV or AUV, to combine the underwater vehicle's speed and water navigation capacity with the manoeuvrability and reach of the HR manipulator. This work advances prior research by integrating data-driven stress prediction with hydrodynamic shape optimisation for underwater HR manipulators while introducing modular buoyancy strategies. Building on prior work in cable-driven HR manipulators (Guardiani et al., 2022; Poka et al., 2024), the proposed manipulator integrates eight lightweight modules, each comprising a single DOF gear joint actuated via cables. Link geometries were optimised by combining Gaussian Process Regression (GPR) (Wilson et al., 2011; Schulz et al., 2018) and Generative Design (GD) (Oh et al., 2019). GPR models are non-parametric probabilistic models that predict outputs by assuming a Gaussian distribution over functions, providing uncertainty estimates. These models have been used extensively in optimisation problems (Boyle, 2007) and various applications such as material sciences (Deringer et al., 2021) and astrophysics (Aigrain and Foreman-Mackey, 2023). GD optimisation uses algorithms to explore and generate high-performance designs by iteratively refining structures based on constraints and objectives (Wang et al., 2023). By training the GPR model on load cases generated using Latin Hypercube Sampling (LHS) (Iman, 2008; Peng et al., 2024), extreme stress scenarios were identified and used to redistribute material via GD, achieving mass and size reductions without compromising structural integrity. This methodology provides structural safety against stochastic underwater loads. Additionally, hydrodynamic efficiency was considered when designing the robot modules, achieving streamlined shapes that reduce hydrodynamic drag. 3D-printed modules were designed and fabricated from Onyx (Markforged Mark, 2025a), a carbon fibre-reinforced Nylon selected for its high strength-to-weight ratio, low density, and minimal water absorption. A test on a two-module prototype submerged in seawater demonstrated near-neutral buoyancy, requiring only minor counterweights for equilibrium. A defining challenge for non-buoyant underwater robots lies in achieving neutral buoyancy while maintaining operational manoeuvrability. Consequently, a second method to achieve buoyancy was provided by designing an external buoyant element for manipulators with a higher density than that of seawater, accounting for printability, density mismatch, and range of motion of the robot joints. This work proposes a simple and scalable framework for field robotics in marine applications, addressing real-world implementation by combining computational optimisation techniques with practical buoyancy and drag management. Potential applications include archaeological recovery, offshore pipeline inspection, ballast tanks, underwater environments of nuclear plants, and ecological monitoring domains where slender, agile manipulators can be advantageous. This manuscript is organised as follows. Section 2.1 outlines the optimisation process. Section 4 presents the 3D-printing, buoyancy design process, and testing. Finally, Section 5 draws the conclusions.

2. Baseline

Adapting an HR manipulator to underwater applications can be challenging, especially if it needs to be carried around by an underwater vehicle. Considering the current state of the manipulator (Guardiani et al., 2022), it would be difficult to attach it to an ROV given its weight and size. The most important part of the system is the actuation unit, which is big compared to the size of a typical ROV, and it would be challenging to carry. Fig. 1 shows the underwater robotic system attached to a typical-sized ROV. This work focuses on the design and optimisation of the robot to make it adaptable to such application. There are two possible approaches to reduce the size and weight of the actuation unit. The first one is to consider an inherently buoyant manipulator made of modules with a density lower than seawater and optimise the structure to reduce the size of the manipulator and improve its hydrodynamic efficiency. The second approach, considered when it is not possible to obtain inherently buoyant modules, is to design external BEs that can decrease the overall density of the system. Both these approaches can decrease the cable tensions needed for actuation, and consequently reduce the actuator's size. Both approaches have been presented in this work and outlined in the following sections.

Table 1
DH parameters of the robot.

Joint	a[mm]	α[rad]	d[mm]	θ[deg]
1	0	$\pi/2$	0	$q_{1,1}$
1_c	65	0	0	$q_{2,1}$
2	160	$-\pi/2$	0	$q_{1,2}$
2_c	65	0	0	$q_{2,2}$
3	16	$\pi/2$	0	$q_{1,3}$
3_c	65	0	0	$q_{2,3}$
4	150	$-\pi/2$	0	$q_{1,4}$
4_c	65	0	0	$q_{2,4}$
5	145	$\pi/2$	0	$q_{1,5}$
5_c	65	0	0	$q_{2,5}$
6	140	$-\pi/2$	0	$q_{1,6}$
6_c	65	0	0	$q_{2,6}$
7	135	$\pi/2$	0	$q_{1,7}$
7_c	65	0	0	$q_{2,7}$
8	135	$-\pi/2$	0	$q_{1,8}$
8_c	65	0	0	$q_{2,8}$
EE	70	0	0	0

2.1. Optimisation process

The existing prototype is shown in Fig. 2.

Table 1 reports the modified DH parameters of the robot, according to Khalil and Dombre (2004), where i_c, with $i = 1, \dots, 8$, represents the constrained revolute joint of the i^{th} module, while EE indicates the end-effector.

In robotics and mechanisms in general, load cases can differ in magnitude, direction, and probability, each influencing a structure's stress, strain, and deformation in distinct ways. Accounting for all relevant load cases is important for designing robust structures that withstand various conditions without compromising safety. This approach also helps avoid both over-design and under-design, providing structural safety while minimising unnecessary material usage. Optimising for multiple load cases presents significant challenges due to the problem's inherent complexity and uncertainty. With potentially hundreds or thousands of load scenarios, or in the case of serial robotic systems, ∞^n, where n is the number of joints, each load combination can have different structural responses. These variations become even more important when considering nonlinear or stochastic behaviours influenced by material properties, geometric factors, or mechanism configurations. Traditional optimisation methods often struggle with this complexity due to the high computational cost and time required for each evaluation, particularly when finite element analysis (FEA) is involved. The optimisation process is based on a method presented in a previous work Poka et al. (n.d.). For each module, the most critical component to optimise is the link, as it is the heaviest part. The length of each link is maintained constant as it is fixed by the DH parameters of the robot. The optimisation process begins with the 8^{th} link and progresses backwards to the first. While this work focuses on optimising the links, the same methodology can be applied to other key components of the robot. First, the LHS algorithm is used to generate $m = 300$ random joint angles for each joint, which results in random robot configurations. The angles of each joint of the robot are fed into the static model to derive the static loads generated by each configuration, considering a payload of 1.5 kg and no gravity acting on the robot modules, as the

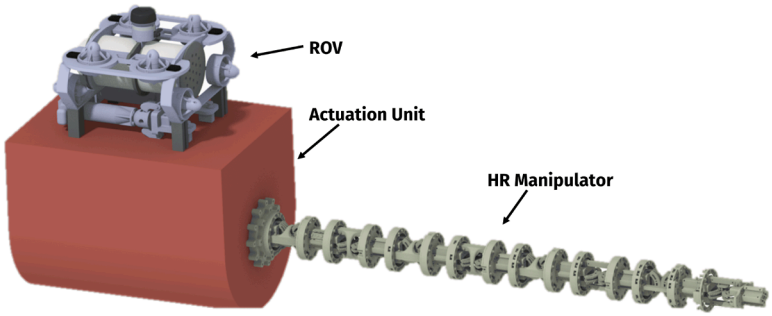

Fig. 1. Concept of the underwater system.

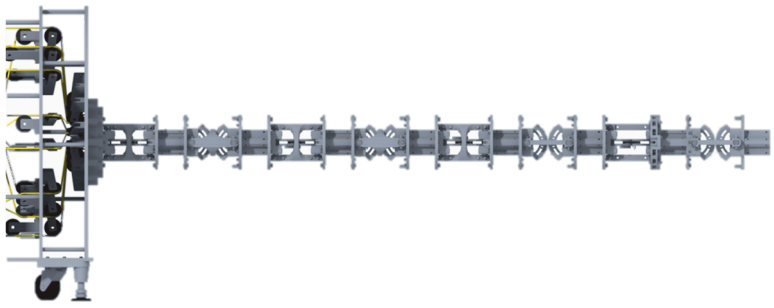

Fig. 2. Virtual prototype model of the existing cable-driven HR manipulator.

robot is meant to be buoyant, which will be shown in the next sections. The result is a matrix of $[m \times length(X)]$ for each joint, where $\mathbf{X} = \{M_{x_i}, M_{y_i}, R_{x_i}, R_{y_i}, R_{z_i}\}$ is the load case vector. Then, the output from the static model is given as input for the structural analysis for all m configurations of the robot. As a result of the structural analysis, a matrix of $m \times X_1$ is obtained, where $\mathbf{X_1} = \{M_{x_i}, M_{y_i}, R_{x_i}, R_{y_i}, R_{z_i}, \sigma_{VM_i}\}$, and σ_{VM_i} represents the Von Mises stress for the i^{th} load combination. The resulting matrix is then used for the training of the GPR model. After the model is trained, new load combinations from the statics model are given as input to the GPR model to predict new stresses and load cases $\mathbf{X}$ and derive the highest one and the corresponding load case, defined as: $\mathbf{X}_{\boldsymbol{\sigma}_{\max}} = \{M_{x_{\sigma_{\max}}}, M_{y_{\sigma_{\max}}}, R_{x_{\sigma_{\max}}}, R_{y_{\sigma_{\max}}}, R_{z_{\sigma_{\max}}}\}$. The next step was the generation of the optimised geometry using the load case found by the GPR algorithm. After the geometry has been generated, the structural validation is performed. For the structural validation, the Extreme Value Analysis (EVA) algorithm was used to obtain the load cases that generate stresses above the threshold t that represents a high confidence limit for extreme but rare load cases, defined as: $\mathbf{X}_{\boldsymbol{\sigma}>t} = \{M_{\sigma>t}, M_{\sigma>t}, R_{\sigma>t}, R_{\sigma>t}, R_{\sigma>t}\}$. If one of these load cases generates stresses that are above the material limit, then generative design is performed again using the said load case, and the process is repeated again. For this case study, no load case has generated stresses above the limit. Each step of this process is outlined in detail in the next sections.

2.2. Multiple load case simulation and stress prediction

To predict extreme stress values and generate unforeseen load cases, the GPR model must be trained on simulation data. Ansys Workbench was employed to perform structural analysis on multiple load cases derived from the static equations for m random configurations generated using the LHS algorithm. For each configuration, the force and moment vector at a given joint is:

$$\mathbf{X} = \{M_{x,m}, M_{y,m}, R_{x,m}, R_{y,m}, R_{z,m}\} \tag{1}$$

where x, y, and z denote directions, and $m = 1, \ldots, 300$ represents configurations. The resulting $m \times 5$ matrix contains different configurations as rows and load components as columns. A Python script automated the process, extracting each row, running Ansys simulations, appending the maximum Von Mises stress per case, and saving the dataset. The next step involved training the GPR model to predict stress for new load combinations based on the simulation data. Unlike deterministic models like neural networks, Gaussian Processes (GPs) provide a probability distribution, with uncertainty estimation (Williams and Rasmussen, 1995; Schulz et al., 2018). Formally, a GP is a set of random variables where any finite subset has a joint Gaussian distribution. The stress response function $f(X)$ is:

$$f(X) \sim \mathcal{GP}(m(X), k(X, X')) \tag{2}$$

where $m(X)$ is the mean function, and $k(X, X')$ is the kernel function (Kanagawa et al., 2018):

$$m(\mathbf{x}) = \mathbb{E}[f(\mathbf{x})], \quad k(\mathbf{x}, \mathbf{x}') = \mathbb{E}[(f(\mathbf{x}) - m(\mathbf{x}))(f(\mathbf{x}') - m(\mathbf{x}'))] \tag{3}$$

with kernel function $K(\mathbf{x}, \mathbf{x}'|\boldsymbol{\tau})$, where $\boldsymbol{\tau}$ is a hyperparameter vector. Large positive values indicate similar inputs, while large negative values indicate dissimilarity.

The GPR model was implemented in MATLAB. The dataset was split into training (80 %) and testing (20 %) via a hold-out cross-validation scheme. Automatic hyperparameter optimisation refined kernel parameters and noise variance, and model performance was validated by comparing predicted stresses to actual values. To explore worst-case scenarios, $p = 1000$ new configurations were generated using LHS and static analysis. The optimisation function was defined as the negative predicted stress to identify the load combination that maximised stress. The *fmincon* algorithm solved this optimisation, with load bounds expanded by 15 % to account for variability in LHS-generated configurations. The optimal load case $\mathbf{X}_{\boldsymbol{\sigma}_{\max}}$ generating the highest predicted stress was identified.

3. Optimal streamlined geometry with generative design

GD is a powerful method to achieve structural efficiency by optimising material distribution based on load path requirements (Mariano et al., 2024). While topology optimization focuses on deriving a single solution by addressing functional objectives, constraints, and loads step-by-step (Sigmund, 2000), GD explores numerous solutions simultaneously, aiming to identify the best options that meet functional and

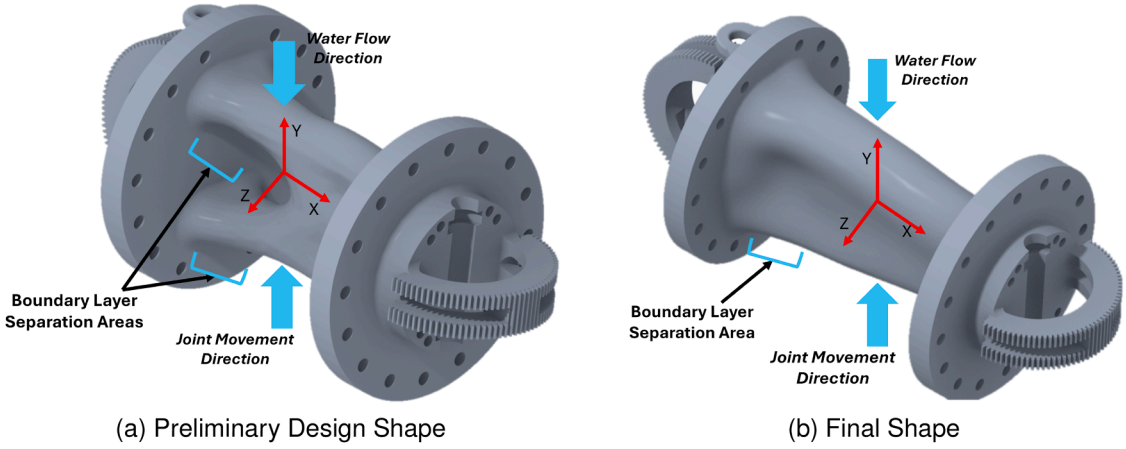

Fig. 3. Shape of the first joint before and after design constraints.

non-engineering requirements. GD aims to determine the optimal distribution of material within a given design space, targeting minimal weight while maintaining structural integrity under multiple load cases (Wu et al., 2019). The GD optimization was performed using Creo Parametric software from PTC, and the steps needed are outlined below. First, the Preserved Geometry (PG) and the Excluded Geometry (EG) need to be specified. PG is the part of the geometry that is part of the analysis, but its shape is not modified. EG is the part of the geometry that is not part of the analysis. Then loads and constraints need to be applied to the PG. In this case, the load case $\mathbf{X}_{\sigma_{\max}}$ coming from the GPR prediction is applied to the PG. If loads need to be applied to the EG, a contact between EG and PG needs to be created first so that the structural analysis can include the constraints applied to the EG. After that, the design criteria need to be specified, which is of two types: stiffness maximization and mass minimization. In this case study, mass minimization was chosen. Then, the design constraints for the geometry generation need to be specified. The design constraints are: the build direction, the parting line, the linear extrude, the build symmetry, the material spreading, and the minimum crease radius. A safety factor of 1.3 was used for the structural optimisation. For a preliminary shape generation, no constraints were imposed on the design criteria, so the generative design algorithm could explore all the available space without constrictions. The generated design is shown in Fig. 3a, where the coordinate system is represented in the local frame.

As the joint rotates around the local Z axis, it is interesting to note that the shape of the link geometry has a higher inertia moment around the Z axis compared to the one about the Y axis. This trend is also seen among all the other joints. This is a desired result since the motion direction of each joint is the direction in which a smaller projection area is needed, resulting in a lower drag coefficient during movement. According to the generated design, the load that affects the stress the most should be R_y, which is why the highest inertia moment of the geometry is I_z. This is demonstrated by:

$$\sigma = \frac{R_y L y}{I_z} \tag{4}$$

Where R_y represents the vertical force applied at one end of a fixed beam with arbitrary cross-section area, L is the distance from the fixed support, y is the distance from the neutral axis, and I_z is the moment of inertia around Z. An increase in I_z can decrease σ. To validate this interesting result, a sensitivity analysis was performed on the load set used for the optimisation to obtain the load that has the highest effect on the stress. The sensitivity analysis is performed using standardized coefficients and is shown in Fig. 4.

The standardized coefficient in a regression model is calculated by transforming the regression coefficients so that they represent the

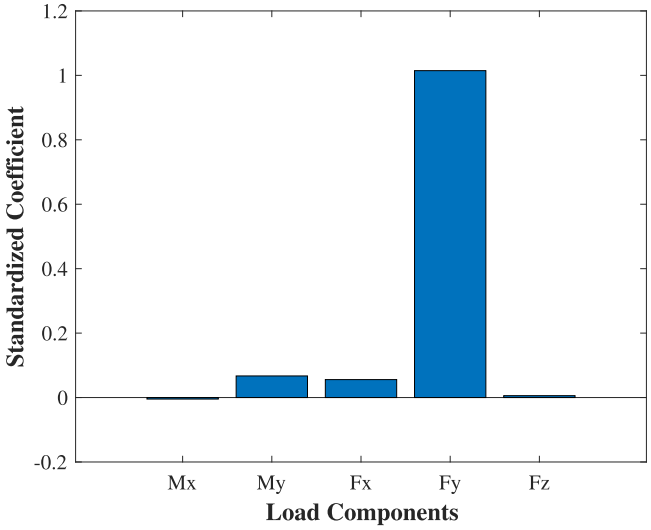

Fig. 4. Sensitivity Analysis on Loads: Standardized Coefficients (Linear Model).

change in the dependent variable in terms of standard deviations. This allows for comparison of the relative importance of each predictor in the model, as all the variables are scaled to have the same units (standard deviations). The standardized coefficient β_{std} is derived as follows:

$$\beta_{std} = \beta \times \frac{\sigma_X}{\sigma_Y} \tag{5}$$

Where β is the unstandardized regression coefficient, σ_{load} is the standard deviation of the predictor variable (load), and σ_{stress} is the standard deviation of the dependent variable (stress). The standardized coefficient reflects the magnitude of the effect of the predictor variable on the dependent variable, making it easier to compare the importance of different predictors in the model. If $\beta_{std} > 0$, it indicates a positive relationship between the predictor variable and the dependent variable (as the predictor increases, the dependent variable also increases). If $\beta_{std} < 0$, it indicates a negative relationship (as the predictor increases, the dependent variable decreases). The coefficient's magnitude reflects the relationship's strength, with larger absolute values indicating stronger effects. The important result from this analysis is that the load R_y has a positive correlation with the stress, and the standardized coefficient is higher in absolute value than that of M_y and F_z. F_x coefficient is not important since F_x does not affect the inertia moment of the geometry, which only depends on the value of

the cross-section area. As is shown in the graph, M_x has a negative correlation coefficient. There may be different reasons for this. These negative values could come from the direction in which the forces or moments are applied, such as opposing the reference axis. The nature of the structural response may lead to a reduction in the system's stress when these loads are increased, thus resulting in negative coefficients.

Having verified that the generated geometry shape is consistent with the static analysis, this advantage was exploited to generate a more streamlined shape, reducing the drag coefficient. A continuous shape geometry is preferred over a discontinuous one to minimise water resistance and drag as it allows for smoother flow around the object, reducing turbulence and pressure drag. When a body moves through water, the surrounding fluid exerts forces that depend on the shape and surface continuity of the object (Cengel and Cimbala, 2013). A continuous geometry ensures that the boundary layer remains attached to the surface for a longer distance, delaying separation and minimising wake formation. In contrast, a discontinuous shape, characterized by abrupt changes, sharp edges, or segmented structures, disrupts the flow, causing early boundary layer separation and increasing pressure drag due to the formation of vortices and turbulent wake regions. By optimising the shape to maintain a gradual pressure gradient along the surface, a continuous design significantly lowers drag forces, reducing the power required for movement in water. For this reason, some constraints are added to the design criteria in the generative design tool, to further adapt the geometry to underwater movement. A double symmetry constraint is applied by forcing the geometry to have symmetry both in the $X-Y$ and $X-Z$ planes. The symmetry in the $X-Y$ plane is needed in order to have a pressure difference close to zero between the two sides of the geometry. The symmetry in $X-Z$ plane is needed to account for the fact that the link can move both upward and downward, this way the drag coefficient difference between the upper and lower side of the geometry is near zero. Another constraint applied to the design criteria is the maximum material spreading, which is reduced to the minimum amount. The reason for this constraint is to reduce boundary layer separations in the geometry, which, as already mentioned, heavily depends on the number of discontinuities in the shape of the object, as illustrated in Fig. 3a. The resulting geometry of the first link is shown in Fig. 3b.

3.1. Optimisation results and validation

After the generation of the optimal geometry is completed, the remaining step is the structural validation of the resulting link geometry for new load conditions. By using the p load cases generated with the GPR model, an Extreme Value Analysis (EVA) (Charras-Garrido and Lezaud, 2013) algorithm was used to determine the stress threshold representing a high confidence limit for extreme but rare load scenarios. Regarding the dataset analysed with the GPR model, the stresses above the threshold are considered for structural analysis on the newly generated geometry, adding an additional layer of confidence for the structural safety of the system. EVA uses a Generalized Extreme Value (GEV) distribution, defined by its cumulative distribution function (Gilleland et al., 2013). For a set of predicted stresses $\sigma_{pred}(X_2)$, the return level σ_{return} is the stress level expected to be exceeded with a specified probability over a given set of configurations. For a given probability level p, the return level is computed as:

$$\sigma_{return} = \mu + \frac{\sigma}{\xi}\left((-\ln(1-p))^{-\xi} - 1\right) \tag{6}$$

where p is the probability level (e.g., 0.99 for a 99 % return level), indicating the likelihood of observing a stress value above σ_{return} within the analysed configurations. Among the $\mathbf{X_2}$ load combinations generated by the GPR model, there are l_i load cases that are above σ_{return}, where i is the link number. A structural analysis was performed on all the l_i load cases on the generated geometry for each link. In this case study, all the robot links withstood the load cases above the corresponding thresholds. However, if one of the links did not resist one of the load cases, the load case that would have caused the link failure would have been considered for another generative design optimisation, and the process of validation would have been repeated.

The resulting optimised prototype has a total mass $m_{tot} = 3.8\ kg$, a length $L = 1.6\ m$, and a payload $P = 1.5\ kg$. The virtual prototype of the optimised robot is shown in Fig. 5. With a payload P, the required torque for the first joint is $M = 16\ Nm$, resulting in a cable tension $F_c = 375\ N$. Inherently buoyant elements allow us to ignore the manipulator weight, as it would not affect the actuation forces, and only the payload can be considered.

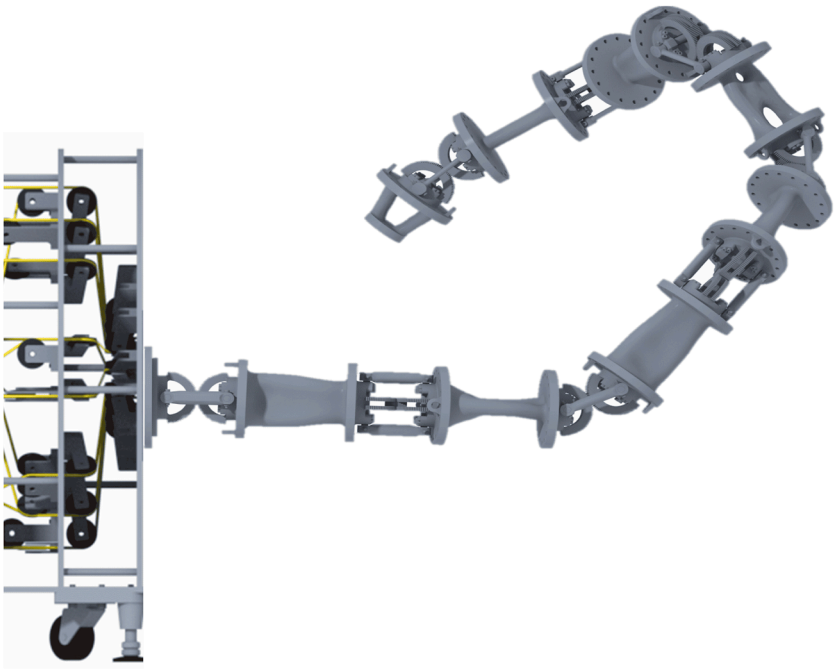

Fig. 5. Virtual prototype of the optimised manipulator.

Table 2
Available 3D printers and specifications.

Printer	Technology	Build Volume [mm]	Accuracy [μ m]
Bambu Lab X1-Carbon (Lab, 2025b)	FDM	256 x 256 x 256	200
Bambu Lab A1 (Lab, 2025b)	FDM	256 x 256 x 256	200
Bambu Lab A1 mini (Lab, 2025b)	FDM	180 x 180 x 180	200
Ultimaker S5 (Ultimaker, 2025b)	FDM	330 x 240 x 300	200 X, Y: ±250 of 25 %
Markforged Mark 2 (Markforged Mark, 2025b)	FDM / CFF	320 x 132 x 154	Z: ±100 of 15 % <1 mm: 30; <50 mm: 70;
Formlabs Form 3 (Formlabs, 2025b)	SLA	145 x 145 x 185	<100 mm: 90; >100 mm: 100 <1 mm: ±30 <50 mm: ±70
Formlabs Form 3B+ (Formlabs, 2025b)	SLA	145 x 145 x 185	<100 mm: ±90 >100 mm: ±100

Table 3
Available materials for each 3D printer.

BambuLab (Lab, 2025a)	Formlabs (Formlabs, 2025a)	Ultimaker S5 (Ultimaker, 2025a)	Markforged Mark 2 (Markforged Mark, 2025a)
		Ultimaker PLA (UPLA)	
		Ultimaker Tough PLA (UTPLA)	
	Form Tough 1500 (FT1500)	Ultimaker ABS (UABS)	
PLA ABS PETG	Form Tough 2000 (FT2000)	Ultimaker PETG (UPETG)	Onyx (Nylon & Carbon Fiber)

Table 4
Material properties provided by the specific printer manufacturers.

	PLA	ABS	PETG	FT1500	FT2000	UPLA	UTPLA	UABS	UPETG	Onyx
Density [g/cm3]	1.24	1.05	1.25	1.05	1.05	1.24	1.24	1.05	1.25	1.20
Tensile Strength Z [MPa]	35 ± 2	28 ±3	38 ± 3	33	46	33	33	19	19	37
Tensile Strength XY [MPa]	39 ± 3	33 ±2	59 ±4			53	45	38	46	71
Water Absorption (saturated) [%]	0.43	0.65	0.30	0.65	0.65					
Heat Deflection Temperature [°C]	57	84	68	52	63	57	57	84	68	145

Considering only the robot weight, the existing prototype needed a minimum cable force of 1180 N at the first joint, which is much higher than F_c, and the actuation unit has been designed accordingly. On the other hand, F_c can be transmitted by a much smaller actuation unit compared to the one used for the existing prototype. Despite the fact that the weight of the manipulator is not important for the actuation, optimisation is still needed to increase the payload-to-size ratio of the system. If the robot is not inherently buoyant, the optimisation method presented is even more important, as a lower weight of the modules results in a lower weight and smaller size of the BEs. This concept is detailed in the next section.

4. 3D Printing, buoyancy design and testing

As mentioned, the optimisation process depends on the buoyancy of the system, which is directly related to the average density of each module. The density of the 3D-printed elements often is not the density of the filament or resin from which it is printed. Generally, SLA printed parts have a higher quality compared to FDM printed ones, as they have fewer void spaces in the material, and consequently, the density of an SLA printed part is usually very close to the theoretical density provided by the manufacturer (Özdilli, 2021). Table 2 shows some of the most widely used and best-performing 3D printers available and their specifications. The build volume is the most important discriminator for the printer choice in this case study. Considering that the maximum dimension of the biggest link of the prototype is around 220 mm, the only suitable printing technology for the links is Fused Deposition Modelling (FDM). The other components of the robot were printed with SLA technology, as it has a better printing quality and the density of the printed parts is closer to the actual density. Table 3 shows the materials with the best mechanical and chemical properties available. The material choice is mainly based on strength, density, and water absorption, in order of importance. Table 4 shows the properties of the available materials for FDM and SLA printing. The data shows that the best-performing materials are FT2000 from Formlabs and Onyx from Markforged Mark 2. The water absorption for Onyx is not easy to obtain since different manufacturers provide different numbers, and the printer manufacturer does not provide any. However, the tensile strength of Onyx is comparable to that of 3D-printed Nylon, and the flexural strength is one of the highest, which is very important for the robot links. Therefore, Onyx is chosen for the links, while FT200 is preferable for the other parts since they are smaller. PETG from BambuLab is also good, but since SLA is preferable, FT2000 is the better choice.

Table 5
Theoretical and real densities of the printed parts.

	SLA Parts	FDM Parts
$\rho_{th}[kg/mm^3]$	1.05	1.2
$\rho_r[kg/mm^3]$	1.03	0.733

4.1. 3D Printing of robot modules and testing

Considering the uncertainties regarding the density of the printed parts, the best approach is to first print the part, with the preferred printing characteristics, whey it, and derive its real density ρ_r calculating the ratio between the measured module weight and the volume of the module provided by the CAD model. After having printed and weighed the parts, and having compared them to the virtual prototypes, the densities of the SLA and FDM printed parts are as shown in Table 5, where ρ_{th} is the theoretical density provided by the manufacturer, and ρ_r is the real measured density.

As shown in Table 5, SLA printed parts have a density that is very close to the theoretical one, while FDM printed parts present a significant density difference. Furthermore, a water absorption test was carried out by submerging one of the modules in seawater for 24 hours. In 3D-printed Nylon parts, most water absorption occurs rapidly within the first day, making it a valid time frame for evaluating the initial effects of moisture absorption before more severe degradation sets in. As reported in Banjo et al. (2022), 3D-printed Nylon can absorb approximately 10 % of its weight in water within the first 24 hours at 21°C, and

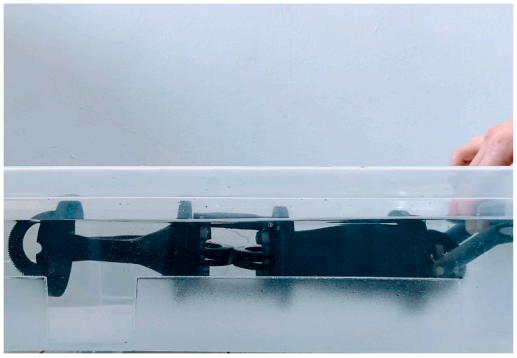

Fig. 6. Buoyancy test on a two-module prototype.

this absorption results in an initial 4 % decrease in yield strength after 24 hours. However, prolonged exposure leads to significant degradation, with a 60 % reduction in flexural modulus after 7 days. Onyx parts are made of Nylon and reinforced by carbon fibre. Hence, the underwater behaviour is considered to be similar, although the carbon fibres may increase the performance, as confirmed by the fact that after 24 hours in submersion, the Onyx parts only gained 3.4 % of their weight. However, a longer submersion time could lead to a non-negligible weight gain and degradation of mechanical properties.

After having assembled the Onyx 3D-printed parts of the first module, it was weighed, and the resulting density was $\rho_a = 1.01\ kg/mm^3$, slightly lower than the seawater density $\rho_w = 1.020\ kg/mm^3$. This difference can be compensated by adding a thin steel ring that wraps around the link or an SLA-printed part that has a high enough density. The optimised 3D-printed parts were assembled into a two-module manipulator and tested for buoyancy, as shown in Fig. 6. The test was performed using seawater from the North Sea, which has a density $\rho_w = 1.020\ kg/mm^3$, which is slightly lower than the world average. The first joint was kept fixed to the outer wall of the bucket to simulate a fixed platform just underneath the water surface height. As shown in Fig. 6, the two modules are almost completely submerged, meaning it is sufficient to add a small counterweight to achieve neutral buoyancy. In this case, it was chosen to leave the robot's average density slightly below water density to account for a slight buoyancy margin for possible non-buoyant end-effectors.

As mentioned in the previous section, if the average density of the i^{th} module is greater than seawater density, which can easily be the case if further assembling components are added or the parts have higher density, an external BE has to be designed for achieving neutral buoyancy. The design process for a generic BE is presented in the next section.

4.2. Design of the external BE

The BEs must be implemented for each module to obtain neutral buoyancy so the whole system stays in equilibrium when in water. The simplest geometry for a BE to be implemented into each link is a hollow cylinder. However, a purely cylindrical shape is not well suited to be 3D printed, no matter the printing technology used, as the part would require internal support in both printing directions, which would increase the mass, and it would be impossible to account for it in the equilibrium equations. This is illustrated in Fig. 7, where Fig. 7a and b show the cylindrical shape in two different view sections. The presented views represent the two possible print directions for the purely cylindrical-shaped geometry. As shown in the figure, in both printing directions, the first geometry needs supports to be printed. In this case study, the BE geometry is considered to be a hollow cylinder with a cone attached to the top, generated by performing a revolution on a triangle, as shown in Fig. 7c. As shown, no supports are needed for the second type of geometry. This is because the side of the triangle is at 50°, which allows printing without needing supports. The material chosen for the BE is ABS, given its low density, which is desirable for having a smaller size.

Fig. 8 shows the cross-section of the geometry, where the crossed-out area indicates presence of material, and, by performing a revolution around the A axis, generates the mentioned shape.

Considering the equilibrium state of each module, the force due to the module's weight must be equal to the hydrostatic force generated by the BE in the opposite direction of gravity. Since it is impossible to fix the BE at the centre of gravity of each module, they will be fixed at the links, as shown in Fig. 9. Adding the BE does not affect the optimisation of the geometry of the link, since it sits entirely outside the link's structural domain.

Depending on the mass of each module and the length of each link, the outer radius R_2 of the cylinder is obtained by solving the equilibrium equation for each module. With reference to Fig. 8, the height H of the BE depends on the link length, while the radius $r_1 = 46\ mm$ is considered slightly above the cable passage radius, and $R_1 = r_1 + t$, $r_2 = R_2 - t$, where $t = 3\ mm$.

$$\rho_w \cdot g \cdot V_{\text{tot-BE}} = g \cdot M_{\text{module}} + \rho_{\text{ABS}} \cdot g \cdot V_{\text{non-void-space-BE}} \tag{7}$$

Where ρ_w is the seawater density considering the average in the North Sea, g is the gravitational constant, $V_{\text{tot-BE}}$ is the total Volume of the BE, M_{module} is the mass of the i^{th} module, ρ_{ABS} is the ABS density, and $V_{\text{non-void-space-BE}}$ is the volume of the non-void space of the BE. The left side of the equation represents the buoyant force, while the right side represents the sum of the weight forces of the i^{th} module and i^{th} BE. With reference to Fig. 8, considering $R_1 = r_1 + t$, V_{tot} and $V_{\text{non-void-space}}$ can be written as:

$$V_{\text{tot}} = \frac{\pi}{4}\tan^2(50°)\left(\tfrac{4}{3}R_2^3 - R_2^2 r_1 - R_2 r_1^2 - \tfrac{1}{3}r_1^3\right) + \pi H\left(R_2^2 - r_1^2\right) \tag{8}$$

$$\begin{aligned} V_{\text{non-void-space}} = {} & \pi H\left(R_2^2 - r_1^2\right) - \pi(H-t)\left(R_2^2 - r_1^2\right) + \frac{\pi}{4}\tan^2(50°) \\ & \left(\tfrac{4}{3}R_2^3 - R_2^2 r_1 - R_2 r_1^2 - \tfrac{1}{3}r_1^3\right) - \frac{\pi}{4}\tan^2(50°) \\ & \left(\tfrac{4}{3}r_2^3 - r_2^2 R_1 - r_2 R_1^2 - \tfrac{1}{3}R_1^3\right) \end{aligned} \tag{9}$$

Rearranging to obtain a third-degree equation, the following can be written:

$$AR_2^3 + BR_2^2 + CR_2 + D = 0 \tag{10}$$

Where:

$$A = \rho_w \frac{\pi}{3}\tan^2(\alpha) - \rho_{\text{abs}}\frac{\pi}{3}\tan^2(\alpha) + \rho_{\text{abs}}\frac{\pi}{3}\tan^2(\alpha),$$

$$\begin{aligned} B = {} & \rho_w \pi H - \rho_w \frac{\pi}{4}\tan^2(\alpha) r_1 - \rho_{\text{abs}}\pi H + \rho_{\text{abs}}\frac{\pi}{4}\tan^2(\alpha) r_1 + \rho_{\text{abs}}\pi H \\ & + \rho_{\text{abs}}\pi t - 2\rho_{\text{abs}}\frac{\pi}{3}\tan^2(\alpha)t - \rho_{\text{abs}}\frac{\pi}{3}\tan^2(\alpha)t - \rho_{\text{abs}}\frac{\pi}{4}\tan^2(\alpha)R_1, \end{aligned}$$

$$\begin{aligned} C = {} & -\rho_w \frac{\pi}{4}\tan^2(\alpha) r_1^2 + \rho_{\text{abs}}\frac{\pi}{4}\tan^2(\alpha) r_1 - 2\rho_{\text{abs}} t\pi H - 2\rho_{\text{abs}}\pi t^2 \\ & + \rho_{\text{abs}}\frac{\pi}{3}\tan^2(\alpha)t^2 + 2\rho_{\text{abs}}\frac{\pi}{3}\tan^2(\alpha)t^2 + \rho_{\text{abs}}\frac{\pi}{4}\tan^2(\alpha)R_1 t \\ & - \rho_{\text{abs}}\frac{\pi}{4}\tan^2(\alpha)R_1^2, \end{aligned}$$

$$\begin{aligned} D = {} & -\rho_w \pi H r_1^2 - \rho_w \frac{\pi}{12}\tan^2(\alpha) r_1^3 + \rho_{\text{abs}}\pi H r_1^2 + \rho_{\text{abs}}\pi H t^2 + \rho_{\text{abs}}\pi t^3 \\ & - \rho_{\text{abs}}\pi H R_1^2 + \rho_{\text{abs}}\pi t R_1^2 + \rho_{\text{abs}}\frac{\pi}{12}\tan^2(\alpha) r_1^3 - \rho_{\text{abs}}\frac{\pi}{4}\tan^2(\alpha) r_1^2 R_1 \\ & - \rho_{\text{abs}}\frac{\pi}{12}\tan^2(\alpha)R_1^3 - \rho_{\text{abs}}\frac{\pi}{3}\tan^2(\alpha)t^3 - \rho_{\text{abs}}\frac{\pi}{4}\tan^2(\alpha)R_1 t^2 \\ & + \rho_{\text{abs}}\frac{\pi}{4}\tan^2(\alpha)t R_1^2 - M_{\text{module}} \end{aligned}$$

Eq. (10) is only valid if the average density of the i^{th} module is higher than the water density.

An important constraint to be considered is the Range Of Motion (ROM) of the joints after the BE implementation. The ROM of each joint depends on the outer radius of the BE, which depends on the weight of the module. Considering an ABS 3D-printed BE, the limit mass of the

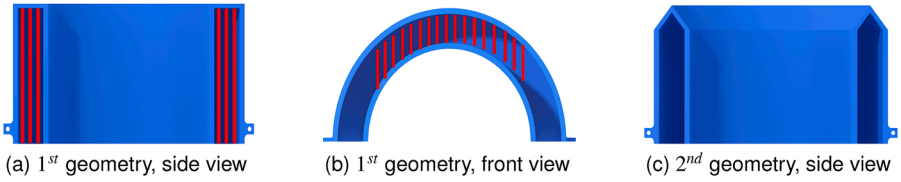

Fig. 7. Comparison between the two possible BE geometries.

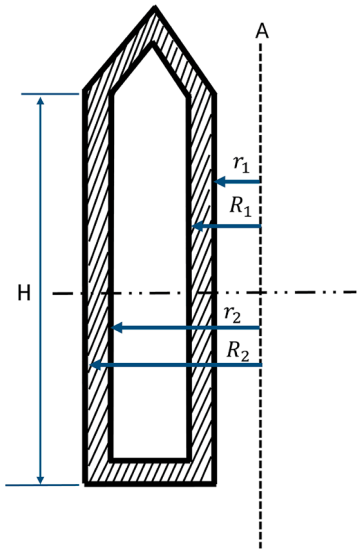

Fig. 8. BE base geometry.

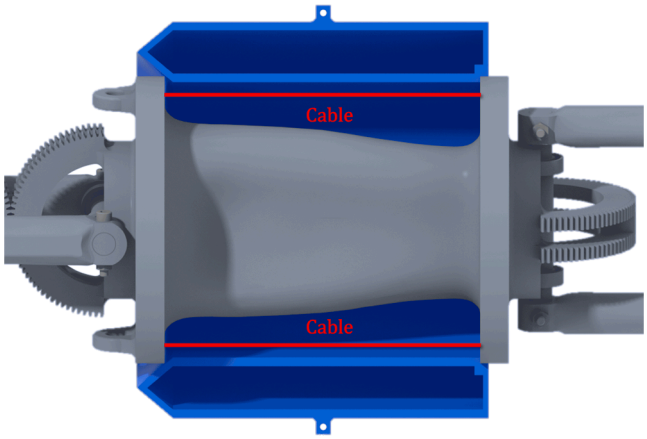

Fig. 9. Implementation of the BE in the modules.

first module allowing a ROM of 45° is 500 g. Given the robot's statics, the modules have decreasing weights toward the tip, with masses never exceeding 500 g, so all the joints allow a ROM of 45°.

4.3. BE testing

The 3D printing material that can be selected for this purpose depends on its density and printing technology, as parts with lower density require a lower buoyant volume. The material selected to test the theoretical derivation is ABS since it has the lowest density among the available materials for 3D printing, resulting in a lighter and smaller BE. To obtain the final BE a test must first be performed on a test part, measuring its weight and deriving its density, as well as testing its water absorption, as it can affect the design. A cube of 3d printed ABS was used for testing. It was weighed before and after having left it in seawater for 24 hours, and the mass change was negligible, around 1.3 %, corresponding to 2 g. Furthermore, the weight of the printed BE was 137 g, while the virtual part showed a weight of 200 g, resulting in a weight loss of 31.5 % after printing. By considering the real weight and the volume of the BE, the real density was measured, obtaining $\rho_a = 0.69$ kg/mm^3. Considering these results, the BE was designed considering the ρ_a of the printed part, and a mass of 600 g was used as module mass, resulting in an outer radius $R_2 = 69.2$ mm. The BE was printed and tested with a 600 g weight, and the result was satisfying, as the system stayed just below the water surface, and when a 10 g non-buoyant mass was added, it began to sink very slowly. This means that the design method for the BE and formulation is correct.

5. Conclusion

This study presents a design framework integrating data-driven stress prediction, generative design topology optimisation, and modular buoyancy strategies to develop a lightweight, tendon-driven hyper-redundant manipulator optimised for underwater applications. The aim of this approach is to optimise the manipulator structure so that it can be used in combination with underwater vehicles such as ROVs. The methodology successfully reduces mass by employing Gaussian processes to predict extreme load cases and generative design to redistribute material while maintaining hydrodynamic efficiency and structural integrity under worst-case static loads. The structural validation process, reinforced by the extreme value analysis method, adds confidence to the design. The fabrication of the manipulator using Onyx, a carbon-fibre-reinforced nylon, enabled near-neutral buoyancy, validated through submerged testing of a two-module prototype, though density mismatches between theoretical and printed parts emphasised the importance of post-fabrication validation. For modules exceeding seawater density, the study introduces buoyant elements designed to account for printability constraints, size, density mismatches, and range of motion limitations. Moreover, by designing custom buoyant elements for each module, rather than applying a generic external buoyant shell, the increase of the external joint envelope is avoided, precise neutral buoyancy tailored to each link's mass distribution is achieved, and equilibrium across the manipulator is maintained. The streamlined geometry of the links has reduced hydrodynamic drag and improved load distribution, aligning with the goal of optimising underwater manoeuvrability. While the methodology provides an effective framework for lightweight and adaptable underwater manipulators, future studies could incorporate computational fluid dynamics simulations, actuator integration to enhance real-world performance, waterproof electronics and actuation systems, and finally experimentation to validate the proposed design. By addressing these challenges, this work contributes a scalable, field-deployable approach for hyper-redundant manipulators in offshore inspection, deep-sea exploration, and other complex marine operations, advancing underwater robotics by combining mechanical efficiency with environmental adaptability.

CRediT authorship contribution statement

Ardit Poka: Writing – original draft, Methodology, Formal analysis, Data curation, Conceptualization; **Daniele Ludovico:** Writing – review & editing, Validation, Supervision; **Federico Manara:** Software;

Lorenzo De Mari Casareto Dal Verme: Writing – review & editing; **Carlo Canali:** Supervision, Resources, Project administration, Investigation, Funding acquisition; **Giovanni Berselli:** Writing – review & editing, Supervision; **Darwin G. Caldwell:** Supervision, Funding acquisition; **Jovana Jovanova:** Supervision, Conceptualization.

Declaration of competing interest

The authors declare that they have no known competing financial interests or personal relationships that could have appeared to influence the work reported in this paper.

Acknowledgment

This work was Partially Funded by the European Union - NextGenerationEU. However, the views and opinions expressed are those of the authors alone and do not necessarily reflect those of the European Union or the European Commission. Neither the European Union nor the European Commission can be held responsible for them. This work was carried out within the framework of the project “RAISE - Robotics and AI for Socio-economic Empowerment” and has been supported by European Union - NextGenerationEU

References

Aguirre-Castro, O.A., Inzunza-González, E., García-Guerrero, E.E., Tlelo-Cuautle, E., López-Bonilla, O.R., Olguín-Tiznado, J.E., Cárdenas-Valdez, J.R., 2019. Design and construction of an ROV for underwater exploration. Sensors 19 (24), 5387.

Aigrain, S., Foreman-Mackey, D., 2023. Gaussian process regression for astronomical time series. Annu. Rev. Astron. Astrophys. 61 (1), 329–371.

Banjo, A.D., Agrawal, V., Auad, M.L., Celestine, A.-D.N., 2022. Moisture-induced changes in the mechanical behavior of 3D printed polymers. Compos. Part C Open Access 7, 100243.

Birk, A., Doernbach, T., Mueller, C., Łuczynski, T., Chavez, A.G., Koehntopp, D., Kupcsik, A., Calinon, S., Tanwani, A.K., Antonelli, G., et al., 2018. Dexterous underwater manipulation from onshore locations: streamlining efficiencies for remotely operated underwater vehicles. IEEE Rob. Autom. Mag. 25 (4), 24–33.

Boyle, P., 2007. Gaussian Processes for Regression and Optimisation. Ph.D. thesis. Open Access Te Herenga Waka-Victoria University of Wellington.

Canali, C., Pistone, A., Ludovico, D., Guardiani, P., Gagliardi, R., De Mari Casareto Dal Verme, L., Sofia, G., Caldwell, D.G., 2022. Design of a novel long-reach cable-driven hyper-redundant snake-like manipulator for inspection and maintenance. Appl. Sci. 12 (7), 3348.

Cengel, Y., Cimbala, J., 2013. Ebook: Fluid Mechanics Fundamentals and Applications (si units). McGraw Hill.

Charras-Garrido, M., Lezaud, P., 2013. Extreme value analysis: an introduction. J. de la société française de Stat. 154 (2), 66–97.

Clark, J., Noonan, D.P., Vitiello, V., Sodergren, M.H., Shang, J., Payne, C.J., Cundy, T.P., Yang, G.-Z., Darzi, A., 2015. A novel flexible hyper-redundant surgical robot: prototype evaluation using a single incision flexible access pelvic application as a clinical exemplar. Surg. Endosc. 29, 658–667.

Deringer, V.L., Bartók, A.P., Bernstein, N., Wilkins, D.M., Ceriotti, M., Csányi, G., 2021. Gaussian process regression for materials and molecules. Chem. Rev. 121 (16), 10073–10141.

Formlabs, 2025a. Formlabs Materials. (accessed 17 March 2025). https://formlabs-media.formlabs.com/filer_public/ac/89/ac8963db-f54a-4cac-8fe9-fb740a7b06f1/formlabs-materials-library.pdf.

Formlabs, 2025b. Formlabs Printers. (accessed 17 March 2025). https://formlabs.com/it/3d-printers/catalog/.

Gilleland, E., Ribatet, M., Stephenson, A.G., 2013. A software review for extreme value analysis. Extremes 16, 103–119.

Guardiani, P., Ludovico, D., Pistone, A., Abidi, H., Zaplana, I., Lee, J., Caldwell, D.G., Canali, C., 2022. Design and analysis of a fully actuated cable-driven joint for hyper-redundant robots with optimal cable routing. J. Mech. Robot. 14 (2), 021006.

Iman, R.L., 2008. Latin hypercube sampling. In: John Wiley Sons, Ltd.

Kanagawa, M., Hennig, P., Sejdinovic, D., Sriperumbudur, B.K., 2018. Gaussian Processes and Kernel Methods: A Review on Connections and Equivalences. arXiv preprint arXiv:1807.02582.

Khalil, W., Dombre, E., 2004. Modeling, Identification and Control of Robots. Butterworth-Heinemann.

Lab, B., 2025a. Bambu Lab Filament Properties. (accessed 17 March 2025). https://bambulab.com/en/filament/guide.

Lab, B., 2025b. Bambu Lab Printers. (accessed 17 March 2025). https://bambulab.com/.

Liljebäck, P., Mills, R., 2017. Eelume: a flexible and subsea resident IMR vehicle. In: Oceans 2017-Aberdeen. IEEE, pp. 1–4.

Lyu, F., Xu, X., Zha, X., Li, Z., Yuan, H., 2022. A snake Eel inspired multi-joint underwater inspection robot for undersea infrastructure intelligent maintenance. In: OCEANS 2022-Chennai. IEEE, pp. 1–6.

Manara, F., Poka, A., Ludovico, D., Pistone, A., De Mari Casareto, D. V.L., Canali, C., Berselli, G., Caldwell, D.G., 2025. Tendon-driven hyper-redundant manipulators: a review on design solutions. IEEE/ASME Trans. Mechatron.

Mariano, F., Pitzalis, R.F., Monica, L., Ortiz, J., Berselli, G., 2024. Traditional vs generative design optimization for novel wrist exoskeleton. In: 2024 20th IEEE/ASME International Conference on Mechatronic and Embedded Systems and Applications (MESA). IEEE, pp. 1–7.

Markforged Mark, ., 2025a. Markforged Mark 2 Onyx. (accessed 17 March 2025). https://markforged.com/materials/plastics/onyx.

Markforged Mark, ., 2025b. Markforged Mark 2 Printer. (accessed 17 March 2025). https://markforged.com/it/3d-printers/mark-two.

Oh, S., Jung, Y., Kim, S., Lee, I., Kang, N., 2019. Deep generative design: integration of topology optimization and generative models. J. Mech. Des. 141 (11), 111405.

Özdilli, Ö., 2021. Comparison of the surface quality of the products manufactured by the plastic injection molding and SLA and FDM method. Int. J. Eng. Res. Dev. 13 (2), 428–437.

Peng, G., Ma, L., Hong, S., Ji, G., Chang, H., 2024. Optimization design and internal flow characteristics analysis based on latin hypercube sampling method. Arabian J. Sci. Eng., 50, 1–40.

Poka, A., Ludovico, D., Manara, F., De Mari Casareto Dal Verme, L., Canali, C., Berselli, G., Caldwell, D.G., Jovanova, J., 2025a. Underwater snake-like robots: a review on design, actuation, and modelling methods. Int. J. Adv. Manuf. Technol., 1–16.

Poka, A., Ludovico, D., Manara, F., De Mari Casareto Dal Verme, L., Canali, C., Berselli, G., Darwin, G.C., Unpublished Results. Structural optimisation of a cable-driven hyper-redundant manipulator. In: 2025 IEEE International Conference on Advanced Intelligent Mechatronics (AIM). IEEE.

Poka, A., Manara, F., Ludovico, D., Pistone, A., De Mari Casareto, D. V.L., Berselli, G., Caldwell, D.G., Canali, C., 2024. Design of a torsional stiffener for a cable-driven hyper-redundant robot composed of gear transmission joints. Int. J. Adv. Manuf. Technol., 136 (9), 3945–3956.

Poka, A., Manara, F., Ludovico, D., Pistone, A., De Mari Casareto, D. V.L., Canali, C., Berselli, G., Caldwell, D.G., 2025b. Alternative solutions to tendon-driven hyper-redundant manipulators: a review on design and actuation strategies. IEEE/ASME Trans. Mechatron.

Rout, S.D., Sutar, M.K., Pattnaik, S., 2020. Design of hyper-redundant in-vivo robot: a review. Trends Mech Biomed.Des. Select Proc. ICMechD 2019, 603–611.

Schulz, E., Speekenbrink, M., Krause, A., 2018. A tutorial on Gaussian process regression: modelling, exploring, and exploiting functions. J. Math. Psychol. 85, 1–16.

Sigmund, O., 2000. Topology optimization: a tool for the tailoring of structures and materials. Phil. Trans. R. Soc. London. Ser. A Math. Phys. Eng. Sci. 358 (1765), 211–227.

Sitler, J.L., Wang, L., 2022. A modular open-source continuum manipulator for underwater remotely operated vehicles. J. Mech. Robot. 14 (6), 060906.

Sverdrup-Thygeson, J., Kelasidi, E., Pettersen, K.Y., Gravdahl, J.T., 2017. The underwater swimming manipulator–OE122800a bioinspired solution for subsea operations. IEEE J. Oceanic Eng. 43 (2), 402–417.

Tang, J., Zhang, Y., Huang, F., Li, J., Chen, Z., Song, W., Zhu, S., Gu, J., 2019. Design and kinematic control of the cable-driven hyper-redundant manipulator for potential underwater applications. Appl. Sci. 9 (6), 1142.

Ultimaker, 2025a. Ultimaker S Series Materials. (accessed 17 March 2025). https://ultimaker.com/materials/s-series-materials/.

Ultimaker, 2025b. Ultimaker S5 Printer. (accessed 17 March 2025). https://ultimaker.com/3d-printers/s-series/ultimaker-s5/.

Wang, Z., Melkote, S., Rosen, D.W., 2023. Generative design by embedding topology optimization into conditional generative adversarial network. J. Mech. Des. 145 (11), 111702.

Williams, C., Rasmussen, C., 1995. Gaussian processes for regression. Adv. Neural Inf. Process. Syst. 8.

Wilson, A.G., Knowles, D.A., Ghahramani, Z., 2011. Gaussian Process Regression Networks. arXiv preprint arXiv:1110.4411.

Wu, J., Qian, X., Wang, M.Y., 2019. Advances in generative design. Comput. Aided Des. 116 (102733), 10–1016.

Yamauchi, Y., Ambe, Y., Nagano, H., Konyo, M., Bando, Y., Ito, E., Arnold, S., Yamazaki, K., Itoyama, K., Okatani, T., et al., 2022. Development of a continuum robot enhanced with distributed sensors for search and rescue. Robomech J. 9 (1), 8.

Zhao, Y., Song, X., Zhang, X., Lu, X., 2020. A hyper-redundant elephant’s trunk robot with an open structure: design, kinematics, control and prototype. Chin. J. Mech. Eng. 33 (1), 1–19.

Zheng, T., Branson, D.T., Guglielmino, E., Kang, R., Medrano Cerda, G.A., Cianchetti, M., Follador, M., Godage, I.S., Caldwell, D.G., 2013. Model validation of an octopus inspired continuum robotic arm for use in underwater environments. J. Mech. Robot. 5 (2), 021004.

Zhou, J., Si, Y., Chen, Y., 2023. A review of subsea AUV technology. J. Mar. Sci. Eng. 11 (6), 1119.